Multi-Contrast CSMRI Using Common Edge Structures with LiGME Model

Daichi Kitahara, Rikako Kato, Hiroki Kuroda, and Akira Hirabayashi
College of Information Science and Engineering, Ritsumeikan University, Shiga, Japan

***Abstract*—CSMRI is the high-speed magnetic resonance imaging (MRI) technique using the compressed sensing (CS) theory. Based on the fact that multiple MR images of different contrasts, e.g., T1-weighted and T2-weighted images, are scanned in clinical practice, Ehrhardt *et al.* proposed multi-contrast CSMRI utilizing the edge information of a different contrast image obtained from the full-sampling k-space data. In this paper, we propose to extend the method of Ehrhardt *et al.* to the *linearly involved generalized Moreau enhanced (LiGME) model*. Since a *directional total variation* based on the edge information becomes closer to a group ℓ_0 pseudo-norm by introducing the LiGME model, we will be able to reconstruct large edges more accurately. Simulations using actual MR images demonstrate the effectiveness of the proposed method.**

***Index Terms*—Multi-contrast MRI, compressed sensing, directional total variation, LiGME model, convex optimization.**

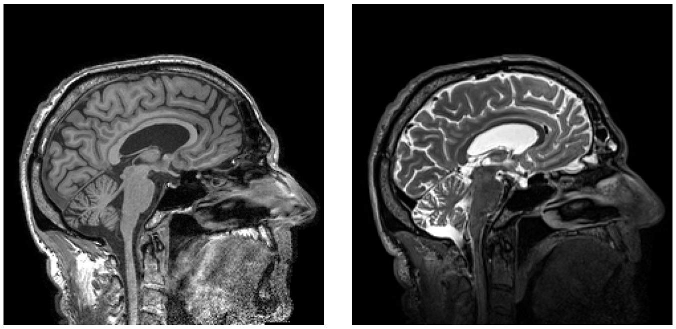
(a) T1-weighted image (b) T2-weighted image

Fig. 1. Structural similarity between T1-weighted and T2-weighted images.

I. INTRODUCTION

Magnetic resonance imaging (MRI) [1]–[3] scans the inside of the human body noninvasively using a strong magnetic field. Compared to X-ray computed tomography (CT) imaging, MRI has the advantage of not exposing patients to X-rays. On the other hand, the disadvantage is that the examination time is relatively long. In clinical practice, multiple types of MR images are scanned by changing the setting of the repetition time (TR) and the echo time (TE) in a single examination. Typical types are T1-weighted and T2-weighted images as shown in Fig. 1. T1-weighted images are good at depicting anatomical structures, while T2-weighted images are suitable for depicting lesions. By comparing such images of different characteristics, a radiologist makes an accurate diagnosis. It takes approximately 2 to 3 minutes to acquire each type of MR image, while CT imaging takes a few seconds. Thus, there is a need to shorten the MRI scanning time for reduction of the burden on patients.

In MRI, the Fourier coefficients of a target slice are observed sequentially in the k-space. Therefore, reducing the number of the observed Fourier coefficients shortens the scanning time. If we apply the inverse Fourier transform, which is the simplest MR image reconstruction method, to such undersampled coefficients, a blurred image containing artifacts is reconstructed. To reconstruct an accurate MR image from the undersampled coefficients, the compressed sensing (CS) theory is used [4]–[12]. CS [13]–[16] is a technique to reconstruct a target signal from a small number of measurements under the assumption that the target signal is sparsely represented in an appropriate space. Based on this theory, Lustig *et al.* proposed a fast MRI method called CSMRI [4], [5]. In this method, a cost function is defined as the sum of a data fidelity term, the ℓ_1 norm of the discrete wavelet coefficients, and the *isotropic total variation*. By minimizing this convex cost function with an iterative algorithm, a clear image can be reconstructed from the undersampled coefficients whose compression rate is about $1/3$.

To improve the image quality, Ehrhardt *et al.* focused on the structural similarity that can be found between different types of MR images on the same slice [10]. As we can see in Fig. 1, although their contrasts are different, edge structures are very similar to each other. Therefore, they proposed a multi-contrast CSMRI method in which the full-sampling is performed only for a single type of MR image, while the Fourier coefficients of other types of images are undersampled so that the entire examination time can be shortened. They defined a *directional total variation* using edges of a reference image obtained from the full-sampling, and then reconstructed the images of different contrasts from the undersampled data by minimizing the sum of the data fidelity term and the directional total variation.

In this paper, to further improve the reconstruction accuracy, we propose to extend the method of Ehrhardt *et al.* to the *linearly involved generalized Moreau enhanced (LiGME) model* [17]. In recent years, Selesnick has proposed the *generalized minimax concave (GMC) function* as an alternative measure of the sparsity to the ℓ_1 norm [18]. The GMC function is continuous but *nonconvex*, and its shape is similar to the ℓ_0 pseudo-norm and the ℓ_p quasi-norm (s.t. $p \in (0, 1)$). Even though the GMC function is *nonconvex*, the sum of the data fidelity term (squared errors) and the GMC function can become *convex* if a matrix parameter of the GMC function is appropriately set. Thanks to the overall convexity, we can reach the global minimum without getting stuck in local minima. Abe *et al.* extended the GMC function, by changing the original cost from

---

This work was supported by JSPS Grants-in-Aid for Early-Career Scientists Grant Number JP19K20361 (e-mail: d-kita@media.ritsumei.ac.jp).

the ℓ_1 norm to any symmetric convex cost, as the *generalized Moreau enhanced (GME) function* [17]. In addition, they proposed the LiGME model that strictly minimizes the sum of the fidelity term and the GME function including a linear mapping. However, it is difficult to design a matrix parameter guaranteeing the overall convexity, and hence the LiGME model has not yet been introduced to relatively large-scale inverse problems.

In the proposed image reconstruction, we first express the directional total variation in [10] as a group ℓ_1 norm including a linear mapping that is the composition of the difference matrix, a rotation matrix and a weight matrix. Second, we replace the group ℓ_1 norm with the GME function while appropriately setting its matrix parameter to guarantee the overall convexity. Third, we modify a proximal splitting algorithm of the LiGME model in [17] so that the constraint set whose projection is easy to compute can be added. Since the directional total variation gets closer to a group ℓ_0 pseudo-norm by the LiGME model, we can reconstruct large edges more accurately. Simulations using the same T1-weighted and T2-weighted images as in [10] demonstrate that the proposed method reconstructs MR images more accurately and quickly than the original method [10].

II. PRELIMINARIES

Let $\mathbb{R}$, $\mathbb{R}_+$, and $\mathbb{C}$ be the sets of all real, nonnegative real, and complex numbers, respectively. The imaginary unit is denoted by $\imath \in \mathbb{C}$. For any $c \in \mathbb{C}$, $\bar{c}$ stands for its complex conjugate. We write vectors with boldface small letters and matrices with capital letters. We express the identity matrix of order N as I_N. The transpose and Hermitian transpose of a vector or a matrix are denoted by $(\cdot)^{\mathrm{T}}$ and $(\cdot)^{\mathrm{H}}$. The positive definiteness and semidefiniteness of a Hermitian matrix $A \in \mathbb{C}^{N\times N}$ are denoted by $A \succ O_N$ and $A \succeq O_N$. For $p > 0$ and a vector $\boldsymbol{x} = (x_1, x_2, \ldots, x_N)^{\mathrm{T}} \in \mathbb{C}^N$, the ℓ_p (quasi-)norm[1] of $\boldsymbol{x}$ is defined as $\|\boldsymbol{x}\|_p := \sqrt[p]{\sum_{i=1}^{N} |x_i|^p}$. For integers G and Q s.t. $GQ = N$, define a group ℓ_1 norm as $\|\boldsymbol{x}\|_{2,1}^{G,Q} := \sum_{i=1}^{Q} \sqrt{\sum_{j=0}^{G-1} |x_{i+jQ}|^2}$.

A. Basic MRI

Among various MRI sequences [1], the two most basic are *spin echo (SE) sequences* and *gradient echo (GRE) sequences*. Although MR images are generally *complex-valued*, the phases greatly vary in the GRE sequences, while there are few phase fluctuations in the SE sequences. This paper uses the model of the *ideal* SE sequences in [10] for simplicity, where each MR image can be modeled as a nonnegative real vector $\boldsymbol{x} \in \mathbb{R}_+^N$.

In the k-space, lattice sampling of the Fourier coefficients is

$$y[k_1, k_2] = \frac{1}{\sqrt{N}} \sum_{n_1=-\frac{N_1}{2}}^{\frac{N_1}{2}-1} \sum_{n_2=-\frac{N_2}{2}}^{\frac{N_2}{2}-1} x[n_1, n_2] e^{-\imath 2\pi \left(\frac{k_1 n_1}{N_1} + \frac{k_2 n_2}{N_2}\right)}, \tag{1}$$

where[2] even numbers N_1 and N_2 s.t. $N_1 N_2 = N$ denote the numbers of vertical and horizontal pixels of an image $\boldsymbol{x}$, $k_1 = -\frac{N_1}{2}, -\frac{N_1}{2}+1, \ldots, \frac{N_1}{2}-1$, $k_2 = -\frac{N_2}{2}, -\frac{N_2}{2}+1, \ldots, \frac{N_2}{2}-1$, and $x[n_1, n_2]$ is the pixel value of $\boldsymbol{x}$. The observation model in (1) is the discretization of an integral [3], and the actual k-space data $y[k_1, k_2] \in \mathbb{C}$ includes both model and observation errors. By concatenating all the observed k-space data $y[k_1, k_2]$ as $\boldsymbol{y}_{\mathrm{full}} \in \mathbb{C}^N$, the observation model in (1) is expressed as

$$\boldsymbol{y}_{\mathrm{full}} = F\boldsymbol{x} + \boldsymbol{\varepsilon}_{\mathrm{full}}, \tag{2}$$

where $F \in \mathbb{C}^{N\times N}$ is the normalized discrete Fourier transform matrix and a noise vector $\boldsymbol{\varepsilon}_{\mathrm{full}} \in \mathbb{C}^N$ includes the two errors.

When the energy $\|\boldsymbol{\varepsilon}_{\mathrm{full}}\|_2^2$ of noise is small, the MR image $\boldsymbol{x}$ can be easily reconstructed with high accuracy by projecting the result $F^{\mathrm{H}}\boldsymbol{y}_{\mathrm{full}}$ of the inverse discrete Fourier transform, for the observed data $\boldsymbol{y}_{\mathrm{full}}$, onto $\mathbb{R}_+^N$ as $P_{\mathbb{R}_+^N}(F^{\mathrm{H}}\boldsymbol{y}_{\mathrm{full}})$.[3] Here the projection $P_{\mathbb{R}_+^N} : \mathbb{C}^N \to \mathbb{R}_+^N$ onto $\mathbb{R}_+^N$ can be computed for any input complex vector by truncating the imaginary parts and replacing negative values of the remaining real parts with zeros.

B. Compressed Sensing MRI (CSMRI)

In MRI, the k-space data $y[k_1, k_2]$ is observed sequentially, not simultaneously. Hence, reducing the number of the observations shortens the scanning time. We observe only M $(< N)$ Fourier coefficients $y[k_1, k_2]$ and concatenate them as a vector $\boldsymbol{y} \in \mathbb{C}^M$. The observation model in CSMRI is expressed as

$$\boldsymbol{y} = F_{\mathrm{u}}\boldsymbol{x} + \boldsymbol{\varepsilon}, \tag{3}$$

where $F_{\mathrm{u}} \in \mathbb{C}^{M\times N}$ is the undersampled Fourier transform matrix, $\boldsymbol{\varepsilon} \in \mathbb{C}^M$ is a noise vector, and $\frac{M}{N}$ is the compression ratio. If we represent the sampling points in the k-space as a binary matrix $S := (s_{i,j}) \in \{0, 1\}^{M\times N}$ s.t. $\sum_{j=1}^{N} s_{i,j} = 1$ for all i and $\sum_{i=1}^{M} s_{i,j} \leq 1$ for all j, then F_{u} is expressed as $F_{\mathrm{u}} = SF$.

Let $\boldsymbol{y}_{\mathrm{pad}} \in \mathbb{C}^N$ be the padded k-space data, where the unobserved coefficients $y[k'_1, k'_2]$ are filled with $\overline{y[-k'_1, -k'_2]}$ or 0.[4] Then, $P_{\mathbb{R}_+^N}(F^{\mathrm{H}}\boldsymbol{y}_{\mathrm{pad}})$ is the simplest reconstruction result,[5] but this cannot be used for diagnosis because of blurring and wrap-around artifacts. In [4], [5], to reconstruct a clear image from the undersampled data $\boldsymbol{y}$, Lustig *et al.* proposed to solve

$$\underset{\boldsymbol{x}\in\mathbb{R}_+^N}{\operatorname{minimize}} \ \frac{1}{2}\|F_{\mathrm{u}}\boldsymbol{x} - \boldsymbol{y}\|_2^2 + \lambda\|\Phi\boldsymbol{x}\|_1 + \mu \mathrm{TV}(\boldsymbol{x}). \tag{4}$$

In (4), the first term is the data fidelity, i.e., squared errors for $\boldsymbol{y}$, and the second and third terms mean the regularizations. In the ideal SE sequences, since $\boldsymbol{x}$ is real-valued, we can use regularization terms similar to those in standard image processing techniques. The matrix $\Phi \in \mathbb{R}^{N\times N}$ denotes a *discrete wavelet transform*, and $\mathrm{TV} : \mathbb{R}^N \to \mathbb{R}_+$ is the *isotropic total variation* computed by $\mathrm{TV}(\boldsymbol{x}) := \sum_{n=1}^{N} \sqrt{\Delta x_{\mathrm{h},n}^2 + \Delta x_{\mathrm{v},n}^2} = \|D\boldsymbol{x}\|_{2,1}^{2,N}$ with the two-dimensional difference matrix $D := [D_{\mathrm{h}}^{\mathrm{T}} \ D_{\mathrm{v}}^{\mathrm{T}}]^{\mathrm{T}}$.[6]

---

[1] Note that the function $\|\cdot\|_p$ satisfies the condition of the norm in $\mathbb{C}^N$ if $p \geq 1$, and the ℓ_0 pseudo-norm of $\boldsymbol{x}$ is defined as $\|\boldsymbol{x}\|_0 := \lim_{p\to+0}\|\boldsymbol{x}\|_p^p$.

[2] In the ideal SE model, $y[0,0], y[0, -\frac{N_2}{2}], y[-\frac{N_1}{2}, 0], y[-\frac{N_1}{2}, -\frac{N_2}{2}] \in \mathbb{R}$ holds. Moreover, for $k_1 \neq -\frac{N_1}{2}$ and $k_2 \neq -\frac{N_2}{2}$, $y[k_1, k_2] = \overline{y[-k_1, -k_2]}$, $y[-\frac{N_1}{2}, k_2] = \overline{y[-\frac{N_1}{2}, -k_2]}$, and $y[k_1, -\frac{N_2}{2}] = \overline{y[-k_1, -\frac{N_2}{2}]}$ also hold.

[3] In the GRE sequences, the reconstructed image is $F^{\mathrm{H}}\boldsymbol{y}_{\mathrm{full}}$. Moreover, in the SE sequences, $\boldsymbol{x}$ can be reconstructed with high accuracy even from almost half $\boldsymbol{y}_{\mathrm{half}}$ of $\boldsymbol{y}$ if we utilize the complex conjugate relations in Footnote 2.

[4] This padding is called the *partial Fourier method* or *half Fourier method*.

[5] In the GRE sequences, the simplest reconstruction is $F^{\mathrm{H}}\boldsymbol{y}_{\mathrm{pad}} := F_{\mathrm{u}}^{\mathrm{H}}\boldsymbol{y}$.

[6] Note that $D_{\mathrm{h}} \in \{-1, 0, 1\}^{N\times N}$ also computes the differences between the left-end and the right-end pixel values. Similarly, $D_{\mathrm{v}} \in \{-1, 0, 1\}^{N\times N}$ computes the differences between the top-end and the bottom-end pixel values.

The parameters $\lambda > 0$ and $\mu > 0$ are weights for the regularization terms. This method gives a good reconstruction result from the observed data whose compression rate is about $1/3$.

C. Multi-Contrast CSMRI Using Common Edge Structures

In clinical practice, a certain part of the body is scanned repeatedly with different settings. Thus, multiple MR images of *different contrasts*, e.g., T1-weighted and T2-weighted images, on the *same slice* are given, and a radiologist makes an accurate diagnosis by comparing them. Ehrhardt *et al.* focused on this diagnostic process, and proposed to use the full-sampling in (2) for a single setting and the undersampling in (3) for other settings, in order to shorten the overall examination time while preserving the image quality [10]. For simplicity, here we acquire a T1-weighted image from the full-sampling $\boldsymbol{y}_{\mathrm{full}}^{\mathrm{ref}} \in \mathbb{C}^N$ while a T2-weighted image from the undersampling $\boldsymbol{y} \in \mathbb{C}^M$. If noise is small, the T1-weighted image can be easily reconstructed with high accuracy as $\boldsymbol{u} := P_{\mathbb{R}_+^N}(F^{\mathrm{H}}\boldsymbol{y}_{\mathrm{full}}^{\mathrm{ref}})$. By using the reconstructed T1-weighted image $\boldsymbol{u}$ as a *reference*, we estimate the T2-weighted image $\boldsymbol{x}$ from its undersampled data $\boldsymbol{y}$.

Ehrhardt *et al.* proposed a multi-contrast CSMRI method as

$$\underset{\boldsymbol{x}\in\mathbb{R}_+^N}{\mathrm{minimize}}\ \frac{1}{2}\|F_{\mathrm{u}}\boldsymbol{x} - \boldsymbol{y}\|_2^2 + \mu\,\mathrm{dTV}(\boldsymbol{x}), \tag{5}$$

where $\mathrm{dTV} : \mathbb{R}^N \to \mathbb{R}_+$ is the *directional total variation* that evaluates the similarity of edges of $\boldsymbol{x}$ and $\boldsymbol{u}$, and is defined by

$$\begin{aligned}\mathrm{dTV}(\boldsymbol{x}) &:= \sum_{n=1}^{N} \left\| (I_2 - \boldsymbol{\xi}_n\boldsymbol{\xi}_n^{\mathrm{T}}) \begin{bmatrix} \Delta x_{\mathrm{h},n} \\ \Delta x_{\mathrm{v},n} \end{bmatrix} \right\|_2 \\ &= \sum_{n=1}^{N} \sqrt{\Delta x_{\mathrm{h},n}^2 + \Delta x_{\mathrm{v},n}^2 - (2 - \|\boldsymbol{\xi}_n\|_2^2)(\boldsymbol{\xi}_n^{\mathrm{T}}\Delta\boldsymbol{x}_n)^2} \end{aligned} \tag{6}$$

with the *horizontal and vertical normalized differences* of $\boldsymbol{u}$:

$$\boldsymbol{\xi}_n := \begin{bmatrix} \xi_{n,1} \\ \xi_{n,2} \end{bmatrix} := \frac{1}{\sqrt{\Delta u_{\mathrm{h},n}^2 + \Delta u_{\mathrm{v},n}^2 + \eta^2}} \begin{bmatrix} \Delta u_{\mathrm{h},n} \\ \Delta u_{\mathrm{v},n} \end{bmatrix}. \tag{7}$$

In (7), a small positive value $\eta > 0$ is added to avoid numerical instabilities. The vector $\boldsymbol{\xi}_n \in \mathbb{R}^2$ is the nth *edge information* of $\boldsymbol{u}$, which is parallel to $\Delta\boldsymbol{u}_n := (\Delta u_{\mathrm{h},n}, \Delta u_{\mathrm{v},n})^{\mathrm{T}} \in \mathbb{R}^2$ and satisfies $0 \le \|\boldsymbol{\xi}_n\|_2^2 < 1$. When $\|\Delta\boldsymbol{x}_n\|_2^2 = \Delta x_{\mathrm{h},n}^2 + \Delta x_{\mathrm{v},n}^2$ is kept constant, $\mathrm{dTV}(\boldsymbol{x})$ takes the minimum if each $\Delta\boldsymbol{x}_n$ is parallel to $\boldsymbol{\xi}_n$ and takes the maximum if $\Delta\boldsymbol{x}_n$ is orthogonal to $\boldsymbol{\xi}_n$. Hence, the T2-weighted image, having common edges with the T1-weighted image, is reconstructed more accurately than (4).

III. MULTI-CONTRAST CSMRI WITH LIGME MODEL

A. Signal Recovery Based on LiGME Model

In signal recovery based on *convex optimization*, we estimate a signal $\boldsymbol{x} \in \mathbb{R}^N$ from an observation $\boldsymbol{y} \in \mathbb{R}^M$ by solving

$$\underset{\boldsymbol{x}\in\mathbb{R}^N}{\mathrm{minimize}}\ \frac{1}{2}\|A\boldsymbol{x} - \boldsymbol{y}\|_2^2 + \mu\Psi(L\boldsymbol{x}), \tag{8}$$

where $A \in \mathbb{R}^{M\times N}$ is an observation matrix, $L \in \mathbb{R}^{K\times N}$ is a linear mapping, and $\Psi : \mathbb{R}^K \to \mathbb{R}$ is a lower semicontinuous convex function. In standard CS-based signal recovery methods [13]–[16], the function Ψ is typically set to the ℓ_1 norm.

While CS aims to reconstruct an unknown sparse signal $\boldsymbol{x}$ from a small number of observations $\boldsymbol{y}$ (s.t. $M < N$), the ℓ_0 pseudo-norm and the ℓ_p quasi-norm (s.t. $p \in (0, 1)$) can more precisely promote the sparsity than the ℓ_1 norm. However, the problem in (8) becomes *nonconvex* when we substitute the ℓ_0 pseudo-norm or the ℓ_p quasi-norm to the regularization term Ψ, and thus finding a global minimizer is challenging.

For the case when the linear mapping L is the identity matrix I_N and the function Ψ is the ℓ_1 norm, Selesnick proposed to use the *generalized minimax concave (GMC) function* [18]:

$$\Psi_B(\boldsymbol{w}) := \Psi(\boldsymbol{w}) - \min_{\boldsymbol{v}\in\mathbb{R}^K} \left[\Psi(\boldsymbol{v}) + \frac{1}{2}\|B(\boldsymbol{w} - \boldsymbol{v})\|_2^2 \right], \tag{9}$$

as an alternative regularization to the ℓ_1 norm, in the form of (8), where a matrix parameter $B \in \mathbb{R}^{J\times K}$ controls the shape of the GMC function. The GMC function Ψ_B is continuous and better approximates the ℓ_0 pseudo-norm than the ℓ_1 norm [18]. Even though the GMC function in (9) is *nonconvex*, the overall problem in the form of (8) is *convex* if the matrix B is appropriately set, and it is possible to find a global minimizer.

Abe *et al.* [17] generalized (9) for any coercive convex function Ψ satisfying $\Psi(-\boldsymbol{w}) = \Psi(\boldsymbol{w})$ for all $\boldsymbol{w} \in \mathbb{R}^K$, and call it the *generalized Moreau enhanced (GME) function*. Moreover, they proposed the *linearly involved GME (LiGME) model*:[7]

$$\underset{\boldsymbol{x}\in\mathbb{R}^N}{\mathrm{minimize}}\ \frac{1}{2}\|A\boldsymbol{x} - \boldsymbol{y}\|_2^2 + \mu\Psi_B(L\boldsymbol{x}). \tag{10}$$

Note that L is an arbitrary matrix in (10). Abe *et al.* clarified a sufficient condition of B for the overall convexity of (10) as

$$A^{\mathrm{T}}A - \mu L^{\mathrm{T}}B^{\mathrm{T}}BL \succeq O_N, \tag{11}$$

and provided a proximal splitting algorithm that successfully obtains a global optimal solution under the condition in (11).

B. Extension of Multi-Contrast CSMRI in (5) to LiGME Model

In this paper, we propose to extend the optimization problem in (5) to the LiGME model for further improvement of the reconstruction accuracy. First, we show that the problem in (5) can be represented in the form of (8). When $\boldsymbol{\xi}_n \neq \boldsymbol{0}$ holds for every n, the directional total variation dTV in (6) is written by

$$\mathrm{dTV}(\boldsymbol{x}) = \sum_{n=1}^{N} \left\| \begin{bmatrix} w_n & 0 \\ 0 & 1 \end{bmatrix} \begin{bmatrix} \frac{\xi_{n,1}}{\|\boldsymbol{\xi}_n\|_2} & \frac{\xi_{n,2}}{\|\boldsymbol{\xi}_n\|_2} \\ -\frac{\xi_{n,2}}{\|\boldsymbol{\xi}_n\|_2} & \frac{\xi_{n,1}}{\|\boldsymbol{\xi}_n\|_2} \end{bmatrix} \begin{bmatrix} \Delta x_{\mathrm{h},n} \\ \Delta x_{\mathrm{v},n} \end{bmatrix} \right\|_2. \tag{12}$$

Note that (12) is a generalized form of dTV in [20] with small positive weights $w_n \in (0, 1]$, and (6) is reproduced by letting $w_n := 1 - \|\boldsymbol{\xi}_n\|_2^2$. From (12), it can be seen that dTV decomposes the horizontal and vertical differences into components parallel and orthogonal to $\boldsymbol{\xi}_n$, and computes the ℓ_2 norm after multiplying each parallel component by the small weight w_n. Furthermore, the condition $\boldsymbol{\xi}_n \neq \boldsymbol{0}$ is not restrictive since we only have to directly compute the ℓ_2 norm of $\Delta\boldsymbol{x}_n$ for n s.t. $\boldsymbol{\xi}_n = \boldsymbol{0}$. Therefore, with the horizontal and vertical difference matrices $D_{\mathrm{h}} \in \{-1, 0, 1\}^{N\times N}$ and $D_{\mathrm{v}} \in \{-1, 0, 1\}^{N\times N}$, an

---

[7] In [19], $(\Psi\circ L)_B(\boldsymbol{x}) := \Psi(L\boldsymbol{x}) - \min_{\boldsymbol{v}\in\mathbb{R}^N}[\Psi(L\boldsymbol{v}) + \frac{1}{2}\|B(\boldsymbol{x}-\boldsymbol{v})\|_2^2]$, similar to $\Psi_B(L\boldsymbol{x}) := \Psi(L\boldsymbol{x}) - \min_{\boldsymbol{v}\in\mathbb{R}^K}[\Psi(\boldsymbol{v}) + \frac{1}{2}\|B(L\boldsymbol{x} - \boldsymbol{v})\|_2^2]$, is also proposed. However, in [19], the authors consider only the denoising, i.e., $A = I_N$, and $\Psi\circ L$ is also restricted to the one-dimensional total variation.

orthogonal matrix $R \in \mathbb{R}^{2N \times 2N}$ corresponding to rotations of $\Delta \boldsymbol{x}_n$, and a diagonal matrix $W \in (0,1]^{2N \times 2N}$ consisting of w_n, the directional total variation dTV can be expressed as

$$\mathrm{dTV}(\boldsymbol{x}) = \left\| WR \begin{bmatrix} D_\mathrm{h} \\ D_\mathrm{v} \end{bmatrix} \boldsymbol{x} \right\|_{2,1}^{2,N} =: \Psi\left(WR \begin{bmatrix} D_\mathrm{h} \\ D_\mathrm{v} \end{bmatrix} \boldsymbol{x} \right),$$

which implies that the problem in (5) is represented by

$$\underset{\boldsymbol{x} \in \mathbb{R}_+^N}{\mathrm{minimize}} \ \frac{1}{2} \| F_\mathrm{u} \boldsymbol{x} - \boldsymbol{y} \|_2^2 + \mu \Psi \left(WR \begin{bmatrix} D_\mathrm{h} \\ D_\mathrm{v} \end{bmatrix} \boldsymbol{x} \right).$$

Based on the above representation in the form of (8) and the discussion in Section III.A, we propose to solve the following optimization problem introducing the LiGME model:

$$\underset{\boldsymbol{x} \in \mathbb{R}_+^N}{\mathrm{minimize}} \ \frac{1}{2} \| F_\mathrm{u} \boldsymbol{x} - \boldsymbol{y} \|_2^2 + \mu \Psi_B \left(WR \begin{bmatrix} D_\mathrm{h} \\ D_\mathrm{v} \end{bmatrix} \boldsymbol{x} \right). \tag{13}$$

From (11), to guarantee the overall convexity of the problem in (13), we have to design the matrix B in (9) satisfying

$$F^\mathrm{H} S^\mathrm{T} S F - \mu \begin{bmatrix} D_\mathrm{h}^\mathrm{T} & D_\mathrm{v}^\mathrm{T} \end{bmatrix} R^\mathrm{T} W B^\mathrm{H} B W R \begin{bmatrix} D_\mathrm{h} \\ D_\mathrm{v} \end{bmatrix} \succeq O_N. \tag{14}$$

This condition is derived by substituting $A := F_\mathrm{u} = SF$ and $L := WRD = WR[D_\mathrm{h}^\mathrm{T} \ \ D_\mathrm{v}^\mathrm{T}]^\mathrm{T}$ in (11). The matrices D_h and D_v are *block circulant with circulant blocks (BCCB)* and thus diagonalizable with the discrete Fourier transform F as $D_\mathrm{h} = F^\mathrm{H} \widehat{D}_\mathrm{h} F$ and $D_\mathrm{v} = F^\mathrm{H} \widehat{D}_\mathrm{v} F$, where $\widehat{D}_\mathrm{h} \in \mathbb{C}^{N \times N}$ and $\widehat{D}_\mathrm{v} \in \mathbb{C}^{N \times N}$ are complex diagonal matrices [6]. Although design of B is difficult especially for a *non-full row rank* L [17], we can design[8] the matrix B satisfying (14), with these expressions, as

$$B = \sqrt{\frac{\theta}{2\mu}} \begin{bmatrix} S \widehat{D}_\mathrm{h}^\dagger F & O_{M \times N} \\ O_{M \times N} & S \widehat{D}_\mathrm{v}^\dagger F \end{bmatrix} R^\mathrm{T} W^{-1} \in \mathbb{C}^{2M \times 2N}, \tag{15}$$

where $\theta \in (0,1]$, and two diagonal matrices $\widehat{D}_\mathrm{h}^\dagger \in \mathbb{C}^{N \times N}$ and $\widehat{D}_\mathrm{v}^\dagger \in \mathbb{C}^{N \times N}$ are the pseudoinverses of $\widehat{D}_\mathrm{h}$ and $\widehat{D}_\mathrm{v}$. Here B in (15) not only satisfies (14) but also can be computed quickly.

C. MR Image Reconstruction Algorithm

The proposed convex optimization problem in (13) is different from the original LiGME model in (10) because the nonnegative constraint $\boldsymbol{x} \in \mathbb{R}_+^N$ is newly imposed. In fact, for such a constrained LiGME model, we can also develop an iterative algorithm that guarantees the convergence to a global optimal solution by slightly modifying the splitting algorithm in [17].

Let $g : \mathbb{C}^N \to \mathbb{R} \cup \{\infty\}$ be a convex function whose *proximity operator* is easily computed, and we consider a problem:

$$\underset{\boldsymbol{x} \in \mathbb{C}^N}{\mathrm{minimize}} \ \frac{1}{2} \| A\boldsymbol{x} - \boldsymbol{y} \|_2^2 + \mu \Psi_B (L\boldsymbol{x}) + g(\boldsymbol{x}).$$

From [17], [21], [22], we can prove that if $\forall \boldsymbol{x} \ \Psi(L\boldsymbol{x}) < \infty$ or $\forall \boldsymbol{x} \ g(\boldsymbol{x}) < \infty$ holds, a global optimal solution is obtained by only adding the computation of $\mathrm{prox}_{\frac{1}{\sigma} g}$ after the update of $\boldsymbol{x}$ of the original algorithm in [17]. Since the proposed optimization problem in (13) corresponds to the case where $A := F_\mathrm{u}$, $L := WRD$, $\Psi := \|\cdot\|_{2,1}^{2,N}$ and g is the *indicator function* of $\mathbb{R}_+^N$, the image reconstruction algorithm[9] is given as

$$\left\lfloor \begin{aligned} \boldsymbol{x}_{k+1} &= P_{\mathbb{R}_+^N} [\boldsymbol{x}_k - \tfrac{1}{\sigma} (A^\mathrm{H} A - \mu L^\mathrm{T} B^\mathrm{H} B L) \boldsymbol{x}_k \\ &\qquad - \tfrac{\mu}{\sigma} L^\mathrm{T} B^\mathrm{H} B \boldsymbol{v}_k - \tfrac{\mu}{\sigma} L^\mathrm{T} \boldsymbol{w}_k + \tfrac{1}{\sigma} A^\mathrm{H} \boldsymbol{y}] \\ \boldsymbol{v}_{k+1} &= \mathrm{prox}_{\frac{\mu}{\tau} \Psi} [\tfrac{\mu}{\tau} B^\mathrm{H} B L (2\boldsymbol{x}_{k+1} - \boldsymbol{x}_k) + \boldsymbol{v}_k - \tfrac{\mu}{\tau} B^\mathrm{H} B \boldsymbol{v}_k] \\ \boldsymbol{w}_{k+1} &= \mathrm{prox}_{\Psi^*} [L(2\boldsymbol{x}_{k+1} - \boldsymbol{x}_k) + \boldsymbol{w}_k] \end{aligned} \right. \tag{16}$$

with $\sigma > 0$ and $\tau > 0$ which satisfy, for some $\kappa > 0$, $\sigma I_N - \frac{\kappa}{2} A^\mathrm{H} A - \mu L^\mathrm{T} L \succ O_N$ and $\tau I_{2N} - \mu(\frac{\kappa}{2} + \frac{2}{\kappa}) B^\mathrm{H} B \succeq O_{2N}$.

IV. NUMERICAL SIMULATIONS

We show the effectiveness of the proposed method by numerical experiments using the T1-weighted and T2-weighted images in Figs. 1(a) and 1(b), which were also used in the simulations of [10]. The number of pixels is $242 \times 242 = 58{,}564 = N$. We used the pixel values after division by 255 and used the sampling mask 'cartesianX_random_0_32' in [10, Fig. 14] that acquires $M = 8{,}480$ Fourier coefficients. Thus, the compression rate is $M/N = 0.1448$, approximately $1/7$. Simulations were conducted on an m-Book T510XN-M2SH5 (Windows 10, Intel Core i7-8750H, 2.20 GHz, 32 GB) by MATLAB R2019a. We compared the proposed method of (13) with the conventional method of (5) in terms of both reconstruction accuracy and computation time. We exploited the code provided in [10] to reproduce the original results of the conventional method.

We first reconstructed the T2-weighted image from the observed data $\boldsymbol{y}$ by using the T1-weighed image as the reference. An initial MR image for both the proposed and conventional methods is generated by the inverse Fourier transform for the padded k-space data $\boldsymbol{y}_\mathrm{pad}$ with the partial Fourier method, as $P_{\mathbb{R}_+^N}(F^\mathrm{H} \boldsymbol{y}_\mathrm{pad})$. Each parameter of the conventional method is well tuned by the code of [10]. For the proposed method, we set the parameters to $\eta = 0.035$ in (7), $w_n := \sqrt{1 - \|\boldsymbol{\xi}_n\|_2^2}$ in (12), $\mu = 0.003$ in (13), and $\theta = \min(\mathrm{diag}(W^2))$ in (15). The step-size parameters σ and τ of the algorithm in (16) are set to

$$\left. \begin{aligned} \sigma &= (\kappa - 1) + \max\Big(\mathrm{diag}\big(\tfrac{\kappa}{2} S^\mathrm{T} S + \mu \widehat{D}_\mathrm{h}^\mathrm{H} \widehat{D}_\mathrm{h} + \mu \widehat{D}_\mathrm{v}^\mathrm{H} \widehat{D}_\mathrm{v}\big)\Big) \\ \tau &= (\kappa - 1) + 0.01\big(\tfrac{\kappa}{2} + \tfrac{2}{\kappa}\big) \max\Big(\big[\boldsymbol{\nu}_\mathrm{h}^\mathrm{T} \ \ \boldsymbol{\nu}_\mathrm{v}^\mathrm{T}\big]^\mathrm{T}\Big) \end{aligned} \right\},$$

where $\kappa = 1.001$, diag gives diagonal components of a square matrix, $\boldsymbol{\nu}_\mathrm{h} = \mathrm{diag}(\widehat{D}_\mathrm{h}^{\dagger\mathrm{H}} S^\mathrm{T} S \widehat{D}_\mathrm{h}^\dagger)$ and $\boldsymbol{\nu}_\mathrm{v} = \mathrm{diag}(\widehat{D}_\mathrm{v}^{\dagger\mathrm{H}} S^\mathrm{T} S \widehat{D}_\mathrm{v}^\dagger)$.

Figures 2(a), 2(b), 2(c), and 2(d) respectively show the target image, the initial image, the result of the conventional method [10], and that of the proposed method, along with an enlarged image of the red boxed area. We can find that the contrast of the reconstructed image by the proposed method in Fig. 2(d) is more clear than that by the conventional method in Fig. 2(c). PSNR and SSIM values are also denoted in the captions. The proposed method improved PSNR by about 1.3 dB and SSIM by 0.02. The computation times for the proposed and conventional methods were 4.22 and 7.85 seconds, respectively. Thus, the proposed method could reconstruct the better image about twice as fast as the conventional method in this simulation.

---

[8] We can fortunately design the matrix B in (15), since not only $F_\mathrm{u}^\mathrm{H} F_\mathrm{u}$ and the difference matrices D_h and D_v can be diagonalized by the discrete Fourier transform F, but also the inverse matrices of R and W are both easily given.

[9] For the *non-ideal* SE sequences where each MR image is a complex vector $\boldsymbol{x} \in \mathbb{C}^N$ having few phase fluctuations, we only have to remove $P_{\mathbb{R}_+^N}$ in (16).

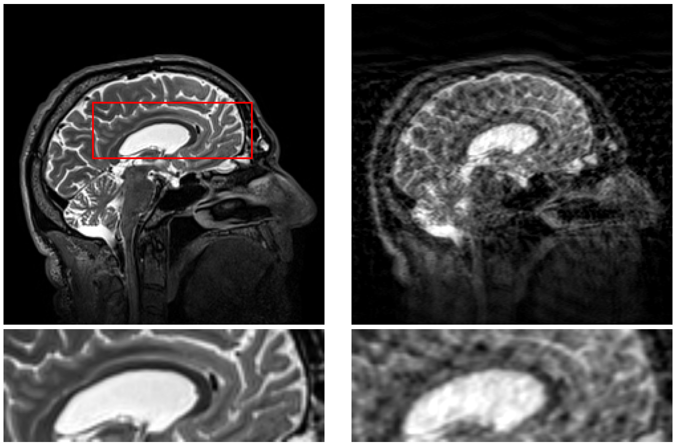

(a) Target image (b) Initial image [22.81 / 0.6027]

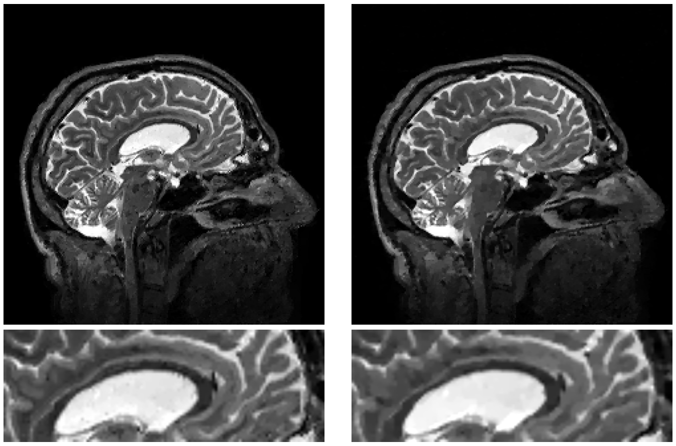

(c) Conventional [26.78 / 0.8648] (d) Proposed [**28.09 / 0.8842**]

Fig. 2. T1-weighted reference & T2-weighted target simulation [PSNR / SSIM].

We also reconstructed the T1-weighted image by using the T2-weighed image as the reference. We used the same values for the parameters of the proposed method. PSNRs of the proposed and conventional methods were 24.43 dB and 23.63 dB, and thus we confirmed that the proposed method was effective in both CSMRI scenarios. Since T1-weighted images describe anatomical structures better than T2-weighed images, the proposed method is suitable for the scenario in which T2-weighted images are reconstructed with T1-weighed reference images.

V. CONCLUSION AND FUTURE WORK

This paper extended the multi-contrast CSMRI method of Ehrhardt *et al.* to the LiGME model for improvement of the reconstruction accuracy. By the LiGME model, the directional total variation based on the edge information of a different contrast image gets closer to a group ℓ_0 pseudo-norm, and the proposed method reconstructs edges more accurately in less computation time, which was shown by simulations. To the best of the authors' knowledge, this work is the first application of the LiGME model to a *large-scale underdetermined* inverse problem. As future work, we plan to integrate the proposed method with parallel imaging techniques [23]–[25] and adapt the proposed method to MR images having large phase fluctuations.

ACKNOWLEDGMENT

We are grateful to Mr. Hiroki Okada and Mr. Yushi Sakakimoto in Kusatsu General Hospital for their valuable advice.

REFERENCES

[1] S. W. Young, *Nuclear Magnetic Resonance Imaging: Basic Principles*. New York, NY, USA: Raven Press, 1984.

[2] P. G. Morris, *Nuclear Magnetic Resonance Imaging in Medicine and Biology*. Oxford, UK: Clarendon Press, 1986.

[3] J. P. Haldar, D. Hernando, S. K. Song, and Z. P. Liang, "Anatomically constrained reconstruction from noisy data," *Magn. Reson. Med.*, vol. 59, no. 4, pp. 810–818, 2008.

[4] M. Lustig, D. L. Donoho, and J. M. Pauly, "Sparse MRI: The application of compressed sensing for rapid MR imaging," *Magn. Reson. Imaging*, vol. 58, no. 6, pp. 1182–1195, 2007.

[5] M. Lustig, D. L. Donoho, J. M. Santos, and J. M. Pauly, "Compressed sensing MRI," *IEEE Signal Process. Mag.*, vol. 25, pp. 72–82, 2008.

[6] Y. Chen, X. Ye, and F. Huang, "A novel method and fast algorithm for MR image reconstruction with significantly under-sampled data," *Inv. Prob. Imaging*, vol. 4, no. 2, pp. 223–240, 2010.

[7] S. Ravishankar and Y. Bresler, "MR image reconstruction from highly undersampled k-space data by dictionary learning," *IEEE Trans. Med. Imaging*, vol. 30, no. 5, pp. 1028–1041, 2011.

[8] C. Tang, N. Inamuro, T. Ijiri, and A. Hirabayashi, "Compressed sensing MRI using double sparsity with additional training images," in *Proc. ICASSP*, New Orleans, LA, USA, 2017, pp. 801–805.

[9] B. Bilgic, V. K. Goyal, and E. Adalsteinsson, "Multi-contrast reconstruction with Bayesian compressed sensing," *Magn. Reson. Med.*, vol. 66, no. 6, pp. 1601–1615, 2011.

[10] M. J. Ehrhardt and M. M. Betcke, "Multicontrast MRI reconstruction with structure-guided total variation," *SIAM J. Imaging Sci.*, vol. 9, no. 3, pp. 1084–1106, 2016.

[11] A. Güngör, E. Kopanoğlu, T. Çukur, H. E. Güven, "Fast recovery of compressed multi-contrast magnetic resonance images," in *Proc. SPIE Med. Imaging*, Orlando, FL, USA, 2017, 6 pages.

[12] P. Song, L. Weizman, J. F. C. Mota, Y. C. Eldar, and M. R. D. Rodrigues, "Coupled dictionary learning for multi-contrast MRI reconstruction," *IEEE Trans. Med. Imaging*, vol. 39, no. 3, pp. 621–633, 2020.

[13] E. J. Candès, J. Romberg, and T. Tao, "Robust uncertainty principles: Exact signal reconstruction from highly incomplete frequency information," *IEEE Trans. Inf. Theory*, vol. 52, no. 2, pp. 489–509, 2006.

[14] D. L. Donoho, "Compressed sensing," *IEEE Trans. Inf. Theory*, vol. 52, no. 4, pp. 1289–1306, 2006.

[15] E. J. Candès, "The restricted isometry property and its implications for compressed sensing," *Comp. Rendus Math.*, vol. 346, pp. 589–592, 2008.

[16] Y. C. Eldar and G. Kutyniok, Eds., *Compressed Sensing: Theory and Applications*. Cambridge, UK: Cambridge University Press, 2012.

[17] J. Abe, M. Yamagishi, and I. Yamada, "Linearly involved generalized Moreau enhanced models and their proximal splitting algorithm under overall convexity condition," *Inv. Prob.*, vol. 36, no. 3, 36 pages, 2020.

[18] I. Selesnick, "Sparse regularization via convex analysis," *IEEE Trans. Signal Process.*, vol. 65, no. 17, pp. 4481–4494, 2017.

[19] I. Selesnick, A. Lanza, S. Morigi, and F. Sgallari, "Non-convex total variation regularization for convex denoising of signals," *J. Math. Imaging Vis.*, vol. 62, no. 6–7, pp. 825–841, 2020.

[20] İ. Bayram and M. E. Kamasak, "Directional total variation," *IEEE Signal Process. Lett.*, vol. 19, no. 12, pp. 781–784, 2012.

[21] L. Condat, "A primal–dual splitting method for convex optimization involving Lipschitzian, proximable and linear composite terms," *J. Optim. Theory Appl.*, vol. 158, no. 2, pp. 460–479, 2013.

[22] L. Condat, D. Kitahara, A. Contreras, and A. Hirabayashi, "Proximal splitting algorithms: A tour of recent advances, with new twists," *preprint arXiv:1912.00137*, 46 pages, 2019.

[23] E. Gong, F. Huang, K. Ying, W. Wu, S. Wang, and C. Yuan, "PROMISE: Parallel-imaging and compressed-sensing reconstruction of multicontrast imaging using sharable information," *Magn. Reson. Med.*, vol. 73, no. 2, pp. 523–535, 2015.

[24] I. Chatnuntawech, A. Martin, B. Bilgic, K. Setsompop, E. Adalsteinsson, and E. Schiavi, "Vectorial total generalized variation for accelerated multi-channel multi-contrast MRI," *Magn. Reson. Imaging*, vol. 34, no. 8, pp. 1161–1170, 2016.

[25] B. Bilgic, T. H. Kim, C. Liao, M. K. Manhard, L. L. Wald, J. P. Haldar, and K. Setsompop, "Improving parallel imaging by jointly reconstructing multi-contrast data," *Magn. Reson. Med.*, vol. 80, pp. 619–632, 2018.